

## Accepted Manuscript

Title: Shape-Selectivity Effects in Syngas-to-Dimethyl Ether Conversion over Cu/ZnO/Al<sub>2</sub>O<sub>3</sub> and Zeolite Mixtures: Carbon Deposition and By-Product Formation

Author: R. Montesano A. Narvaez D. Chadwick



PII: S0926-860X(14)00333-0  
DOI: <http://dx.doi.org/doi:10.1016/j.apcata.2014.05.009>  
Reference: APCATA 14829

To appear in: *Applied Catalysis A: General*

Received date: 5-11-2013  
Revised date: 22-4-2014  
Accepted date: 10-5-2014

Please cite this article as: R. Montesano, A. Narvaez, D. Chadwick, Shape-Selectivity Effects in Syngas-to-Dimethyl Ether Conversion over Cu/ZnO/Al<sub>2</sub>O<sub>3</sub> and Zeolite Mixtures: Carbon Deposition and By-Product Formation, *Applied Catalysis A, General* (2014), <http://dx.doi.org/10.1016/j.apcata.2014.05.009>

This is a PDF file of an unedited manuscript that has been accepted for publication. As a service to our customers we are providing this early version of the manuscript. The manuscript will undergo copyediting, typesetting, and review of the resulting proof before it is published in its final form. Please note that during the production process errors may be discovered which could affect the content, and all legal disclaimers that apply to the journal pertain.

## Highlights

- Syngas-to-DME over Cu/ZnO/Al<sub>2</sub>O<sub>3</sub> and zeolites with different channel dimensionality
- Theta-1 and ferrierite have the highest selectivity to DME
- Nature of entrained organics dictates distribution of hydrocarbon by-products
- Structures with spatial constraints more resistant to coke formation

Accepted Manuscript

## Shape-Selectivity Effects in Syngas-to-Dimethyl Ether Conversion over Cu/ZnO/Al<sub>2</sub>O<sub>3</sub> and Zeolite Mixtures: Carbon Deposition and By-Product Formation

R. Montesano, A. Narvaez<sup>‡</sup> and D. Chadwick\*

Department of Chemical Engineering, Imperial College London, South Kensington Campus, SW7 2AZ, London, United Kingdom

\* Corresponding author. Tel: +44 20 7594 5579. E-mail address: d.chadwick@imperial.ac.uk

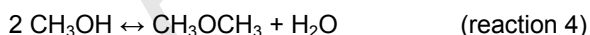
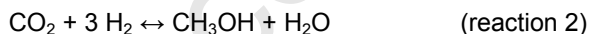
### Abstract

The conversion of syngas into dimethyl ether has been studied over physical mixtures of a Cu/ZnO based catalyst and a zeolite. Theta-1, ZSM-23, ferrierite, ZSM-5 and mordenite were used. The zeolites were separated after reaction and characterised by temperature programmed oxidation, XRD, and GC-MS of the entrained hydrocarbons. Theta-1 and ferrierite were found to have the most stable performance and the highest selectivity to DME. Deactivation is shown to be faster for structures with enough space to accommodate bulky carbonaceous deposits such as mordenite and ZSM-5. Longer diffusion paths associated with larger crystallites also contributed to rapid loss of activity for ZSM-23. The zeolite topology was found to influence the nature of the entrained alkylbenzenes.

### 1. Introduction

Increasingly stringent environmental regulations have prompted research on the development of alternative clean fuels. In this context, dimethyl ether (DME) appears as a promising substitute for diesel in compression ignition engines due to its high cetane number. The efficiency, power and torque of the engines fuelled with DME are similar to diesel engines, while SO<sub>x</sub>, NO<sub>x</sub> and particulate matter emissions are suppressed or significantly reduced [1]. In addition DME can be used in direct oxidation fuel cells with the advantages of pumpless delivery and high energy density storage [2].

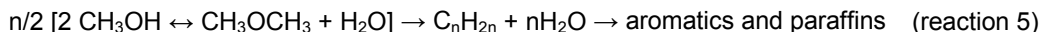
The single-stage synthesis of dimethyl ether from syngas has attracted attention due to the increased once-through conversion compared to the methanol only production. This process requires the combination of two catalytic functions: hydrogenation of carbon oxides to methanol (reactions 1 to 3) and methanol dehydration (reaction 4). In addition to the lower thermodynamic constraints resulting from the transformation of methanol into less limiting DME, under typical CO rich conditions the water produced in reaction 4 is transformed into CO<sub>2</sub> and H<sub>2</sub> by reaction 3. This favours the kinetics of the methanol synthesis (reaction 2) and reduces the demand of hydrogen in the process.



While Cu/ZnO/Al<sub>2</sub>O<sub>3</sub> is a well-established methanol synthesis component, many solid acids appear as candidates for the dehydration step including  $\gamma$ -alumina, and zeolites ZSM-5, ferrierite and Y zeolite [3-5].  $\gamma$ -Alumina exhibits a remarkable selectivity towards DME [3] but zeolites show better performance in terms of catalytic activity and stability, especially in the presence of water [4].

<sup>‡</sup> Present address: Facultad de Ingeniería, Universidad Católica de la Santísima Concepción, Alonso de Ribera 2850, Concepción, Chile

Dimethyl ether is an intermediate product in the transformation of methanol-to-hydrocarbons (MTH). The overall reaction path of methanol conversion to olefins and other hydrocarbons can be summarised as:



MTH processes are normally conducted between 350°C and 400°C at atmospheric pressure. The conversion and the selectivity depend on the strength and the density of the acid sites, the residence time and the reaction temperature [6]. It has been recognised that the topology of the zeolites (shape-selectivity) strongly affects the product distribution in MTH processes [7]. Mordenite (MOR), for instance, has a pore structure formed by elliptical channels of 12 atom-rings (6.7 x 7.0 Å) interconnected by 8 atom-ring cages (2.9 x 5.7 Å). Its relatively wide pores readily accommodate oligomers and aromatics that tend to be the main products of methanol dehydration. Adsorption of these products over the strong acid sites eventually leads to the blockage of the cages causing very fast deactivation [8]. On the other hand, the intersections of the medium-size channels of ZSM-5 provide space for cyclization and intermolecular hydride transfer reactions. The pores are wide enough to diffuse even tetramethylbenzene (5.1 x 5.4 Å and 5.4 x 5.6 Å) so the typical products of methanol dehydration over H-ZSM-5 include olefins, aromatics and paraffins [9]. For ferrierite (FER), the diameter of the main channels is about 10% smaller than those of ZSM-5 and the pores are interconnected by 8 atom-ring cages (4.2 x 5.4 Å and 3.5 x 4.8 Å) slightly bigger than those of mordenite. The space in the cages is not enough to form aromatics or paraffins so light olefins are selectively produced [9]. Similar results have been obtained with SUZ-4, which is structurally related to ferrierite [10]. 10 atom-ring one-directional zeolites such as theta-1 (5.7 x 4.3 Å) and ZSM-23 (5.2 x 4.5 Å) have been reported to produce mainly aromatic-free C<sub>5+</sub> hydrocarbons since the narrow pores impede the formation of aromatics to a significant extent [11].

While shape-selectivity has been extensively studied in methanol-to-hydrocarbon processes, few reports exist on shape related effects in the combined synthesis and dehydration of methanol from syngas to form DME. Under syngas-to-DME conditions (240-270°C and 30-50 bar) the pore structure of the zeolites can be expected to be crucial in limiting hydrocarbon formation without detriment to the DME productivity. Sai Prasad et al. [12] reported higher stability and selectivity to DME of H-FER composite catalysts compared to H-ZSM-5 and H-Y in the single-stage or “direct” production of DME from syngas. The results were interpreted in terms of the catalyst topology facilitating the diffusion of the reactants and the products to and from the active sites. The influence of the channel structure was also used by Pais da Silva and co-workers to explain the absence of hydrocarbon by-products in spite of the high dehydrogenation activity of H-ferrierite [13, 14]. Similarly, Jiang et al. [10] ascribed the high stability of DME synthesis over SUZ-4 to the absence of catalytic sites for the dehydration of DME to hydrocarbons.

Recently, García-Trenco et al [15] reported an extensive study addressing the impact of the zeolite topology on the performance of hybrid catalysts in syngas-to-DME conversion. They used 10 atom-ring bi- and tri-dimensional structures (ZSM-5, FER, MCM-22, IM-5 and TNU-9) and the delaminated MWW structure, ITQ-2, all with Si/Al ratios around 10. The authors studied the direct dehydration of methanol over the zeolites alone at atmospheric pressure and found that deactivation was caused by carbonaceous deposits whose nature depended on the topology of the zeolite used. On the other hand, the loss of activity for the hybrids was found to be related mainly to the aluminium content in the exterior of the zeolite crystallites. This was explained by a detrimental interaction between the Cu/ZnO component and the proton-exchange positions located on the external surface of the acid catalyst.

The present paper reports shape-related effects on syngas-to-DME conversion using different zeolites physically mixed with Cu/ZnO/Al<sub>2</sub>O<sub>3</sub> catalyst particles. The use of physical mixtures allows the independent characterisation of the mixture components after reaction in contrast to the case of hybrids such as those studied recently [15]. In principle, depending on the crystallite sizes, it can also

minimise the effect of the direct contact between the catalyst components. As a consequence, the study of the intrinsic causes of deactivation of the zeolites under the applied STD conditions is facilitated. The main focus of the present work is use of the medium pore unidirectional structures theta-1 and ZSM-23 in the physical mixtures, and ferrierite (medium and small size bidirectional pores), which affords direct comparison with recent work on hybrids [12,15] and earlier studies [11], and the impact of the pore structure on their deactivation. These zeolites are contrasted with the behaviour of mordenite (large pseudo-unidirectional pores), and ZSM-5 (medium size three-dimensional structure) which have been widely studied for methanol-to-hydrocarbons and syngas-to-DME processes both in hybrids [5,12,15] and in physical mixtures [16,17]. Except for mordenite, all the zeolites were selected to have similar  $\text{SiO}_2$  to  $\text{Al}_2\text{O}_3$  molar ratios to avoid large differences in acidity. The distribution of hydrocarbons obtained as by-products in the syngas-to-DME conversion is also studied. The studies reported here were conducted under strongly reducing conditions with a methanol forming/dehydration component ratio of 1:1 (wt:wt) and at low CO conversions. These conditions enhance the influence of the kinetics of the reactions particularly the dehydration reaction, on the overall production of DME and reduce the potential for mediation of deactivation by high water partial pressures.

## 2. Experimental methods

### 2.1 Catalyst preparation

Theta-1 and ZSM-23 were synthesised following the procedure reported by Barri et al. [18, 19]. The dried as synthesised zeolites were calcined in air at  $550^\circ\text{C}$  to remove the organic template and then ion-exchanged with a concentrated solution of ammonium nitrate. Ferrierite (CP 914), ZSM-5 (CBV 5524G) and mordenite (CBV 21A) were purchased from Zeolyst International. The zeolite powders were pressed into tablets (with no lubricant or binder), crushed and sieved to granules in the size range of 250 to 500  $\mu\text{m}$ . Subsequently, the particles were calcined for 6 hours in flowing air to obtain the proton form of the zeolites.

A commercial  $\text{Cu/ZnO/Al}_2\text{O}_3$  based catalyst (HiFuel R120, Johnson Matthey) was used as methanol synthesis component. It was also crushed and sieved to granules in the size range of 250 to 500  $\mu\text{m}$ .

### 2.2 Catalyst characterisation

X-ray powder diffraction (XRD) was done in a PANalytical X'Pert Pro diffractometer (Cu  $K\alpha$  radiation) at room temperature and in the reflection mode. The surface morphology of the zeolites was examined by scanning-electron microscopy (SEM) using a Zeiss Auriga FIB/FES-SEM microscope. Continuous-wave electron paramagnetic resonance (EPR) was conducted at room temperature and at 50 K in a Bruker E560D-P instrument operating in the X-band with microwave attenuation of 30 dB and modulation amplitude of 5 G. BET surface areas and pore volumes were determined by physisorption of  $\text{N}_2$  at 77K using a Micrometrics TriStar 3000 instrument. Desorption isotherms were used to calculate the pore volumes following the BJH method. The external surface area of the zeolites was calculated by subtracting the micropore area obtained using the t-plot approach from the BET specific surface area.

Temperature programmed desorption of ammonia ( $\text{NH}_3$ -TPD) and temperature programmed oxidation (TPO) were conducted in a stainless steel micro-flow reactor (ID = 0.45 mm) heated by a concentric electric furnace. The eluted gases were analysed using a quadrupole mass spectrometer with a heated capillary. For  $\text{NH}_3$ -TPD the zeolites (0.1 g) were pretreated in situ at  $550^\circ\text{C}$  flowing 40  $\text{mL}\cdot\text{min}^{-1}$  of He for 1 h and then cooled down to the adsorption temperature ( $110^\circ\text{C}$ ). A mixture 5%  $\text{NH}_3$  in He was fed for 30 min keeping the volumetric flow rate of the pretreatment. After the ammonia was purged, desorption proceeded under flowing He (40  $\text{mL}\cdot\text{min}^{-1}$ ) increasing the temperature up to  $660^\circ\text{C}$  at a rate of  $10^\circ\text{C}\cdot\text{min}^{-1}$ . TPO was conducted using 20 mg of the sample and flowing 45  $\text{mL}\cdot\text{min}^{-1}$

<sup>1</sup> of a mixture 10% O<sub>2</sub> in Ar. The temperature was then increased from room temperature to 800°C at 10°C·min<sup>-1</sup>.

### 2.3 Activity tests

A continuous microflow reactor system was used with a stainless steel tubular fixed-bed reactor (ID = 9.5 mm, length = 300 mm) heated by a concentric aluminium furnace block. H<sub>2</sub> and CO in a ratio 2:1 were supplied via mass flow controllers and passed through sulphur (activated carbon) and carbonyl ( $\alpha$ -Al<sub>2</sub>O<sub>3</sub> at 200°C) traps before entering the reactor. The  $\alpha$ -Al<sub>2</sub>O<sub>3</sub> bed is also used to preheat the syngas. Online gas chromatography (FID, TCD) was used to analyse the products. Argon was added to the feed gas as an internal reference for the gas analysis. The exit lines were trace heated to prevent condensation. A heated backpressure regulator was used to maintain the pressure. Physical mixtures of Cu/ZnO/Al<sub>2</sub>O<sub>3</sub> and acid component (250-500  $\mu$ m) were diluted with inert silicon carbide (764  $\mu$ m) to give a volume ratio 1:2:3 and a catalyst bed volume of 1.5 mL which was placed between pre- and post-packing (0.25 mL) of SiC. The catalyst mixtures were activated in situ by reduction in 10% H<sub>2</sub>/N<sub>2</sub> (100 mL·min<sup>-1</sup>) at 210°C and atmospheric pressure for 12 hours and then increased to the reaction temperature at 1°C·min<sup>-1</sup> in 10% H<sub>2</sub>/N<sub>2</sub> and held for 1 hour before introduction of syngas. All the experiments were conducted at 3 MPa with a GHSV of 8400 h<sup>-1</sup> based on the catalyst bed volume. Each experiment had three periods with different reaction temperatures: 250°C (9 hours), 260°C (15 hours) and 270°C (8 hours) run consecutively. After each period, the following reaction temperature was approached at a rate of 1°C·min<sup>-1</sup>. Blank experiments conducted in the absence of catalysts or with the acid component alone gave negligible syngas conversions.

Comparison of the carbon balance obtained from FID and TCD showed average deviations below 5%. The CO conversion,  $X_{CO}$ , and the selectivity towards methanol, dimethyl ether, CO<sub>2</sub> and hydrocarbons,  $S_{MeOH}$ ,  $S_{DME}$ ,  $S_{CO_2}$ ,  $S_{HC}$  were calculated as follows:

$$X_{CO} = \frac{F_{CO}^{in} - F_{CO}^{out}}{F_{CO}^{in}} \quad (1)$$

$$S_{MeOH} = \frac{F_{MeOH}^{out}}{F_{CO}^{in} - F_{CO}^{out}} \quad (2)$$

$$S_{DME} = \frac{2 \cdot F_{DME}^{out}}{F_{CO}^{in} - F_{CO}^{out}} \quad (3)$$

$$S_{CO_2} = \frac{F_{CO_2}^{out}}{F_{CO}^{in} - F_{CO}^{out}} \quad (4)$$

$$S_{HC} = \frac{\sum \eta_i F_{HC,i}^{out}}{F_{CO}^{in} - F_{CO}^{out}} \quad (5)$$

where  $F_{CO}^{in}$  is the inlet molar flow rate of CO;  $F_{CO}^{out}$ ,  $F_{MeOH}^{out}$ ,  $F_{DME}^{out}$ ,  $F_{CO_2}^{out}$  and  $F_{HC,i}^{out}$  are the outlet molar flow rates of CO, methanol, DME, CO<sub>2</sub> and the corresponding hydrocarbon. The number of carbon atoms in the hydrocarbon molecule is expressed by  $\eta_i$ .

### 2.4 Analysis of the material retained in the zeolites

After reaction, the zeolites were separated from the physical mixture except for mordenite for which visual differentiation of the heavily coked particles was not possible. The samples (15 mg) were digested using 0.5 mL of 20% HF and the carbonaceous compounds were extracted with an equal volume of  $\text{CH}_2\text{Cl}_2$  according to the method proposed by Guisnet et al. [20]. Subsequently, the organic phase was analysed using an HP-6890 gas chromatograph with an Agilent-5973 mass selective detector (GC-MS).

### 3. Results and discussion

#### 3.1 Catalyst characterisation

The X-ray diffraction patterns of the zeolites are presented in Fig. 1. No crystalline impurities were found and the structures were entirely consistent with the known patterns. The surface areas and micropore volumes, Table 1, are in agreement with values in the literature and with the supplier data sheets [21, 22]. The nominal composition is in the range of  $\text{SiO}_2/\text{Al}_2\text{O}_3$  from 50-68 except for mordenite ( $\text{SiO}_2/\text{Al}_2\text{O}_3 = 20$ ).  $\text{NH}_3$ -TPD of the fresh zeolites in their proton form gave two desorption peaks as shown in Fig. 2. The high temperature peak is associated with ammonia adsorbed on the framework acid sites (Brønsted sites), while the low temperature peak corresponds to  $\text{NH}_3$  molecules that are hydrogen bonded to those chemisorbed within the micropores or associated with extra-framework aluminium species [23]. The amount of  $\text{NH}_3$  desorbed from the zeolites was calculated after deconvolution of the low temperature (LT) and high temperature (HT) peaks and is given in Table 2. The amount of  $\text{NH}_3$  desorbed in the HT peak corresponds well with the  $\text{H}^+$  concentration calculated from the  $\text{SiO}_2/\text{Al}_2\text{O}_3$  ratios with the exception of mordenite possibly because desorption is not complete at the maximum temperature used. The location of the high temperature peak maxima in Fig. 2 reflects the average heat of adsorption of ammonia over each zeolite so the acid strength of the samples follows the general trend: MOR > FER > ZSM-23  $\geq$  theta-1  $\approx$  ZSM-5, (with the provision that the channel structure of the zeolites may impose constraints on the diffusion of the desorbing molecules, affecting the shape and the location of the desorption peaks).

The nitrogen physisorption isotherms for ferrierite, theta-1 and ZSM-23 are shown in Fig. 3. The profiles of MOR and ZSM-5 are given in the supplementary information (Fig. D and E). Adsorption occurs mainly at very low relative pressures ( $p/p_0$ ) as expected for microporous solids. Ferrierite, mordenite and theta-1 exhibit an almost reversible adsorption-desorption behaviour up to  $p/p_0 = 0.8$ , while both ZSM-5 and ZSM-23 present clear hysteresis. In the case of ZSM-5, the loop is ascribed to capillary condensation taking place above  $p/p_0 \sim 0.4$  [24]. For ZSM-23, hysteresis is caused by a uniform porosity originated within agglomerates of particles of similar size and shape [25]. From Fig. 3 it is also evident that ZSM-23 is a purely microporous zeolite showing  $\text{N}_2$  adsorption at low relative pressures ( $p/p_0$ ) followed by a plateau. On the contrary, ferrierite and theta-1 adsorb  $\text{N}_2$  in the micropore region but the uptake continues in the mesopore range. SEM images reveal that the mesoporosity arises from intercrystalline voids resulting from the small size and the shape of theta-1 ( $< 0.2 \mu\text{m}$ , nanorods) and FER ( $< 0.8 \mu\text{m}$ , plates), as opposed to the rather large crystallites of ZSM-23 ( $> 1 \mu\text{m}$ , rods), Fig. 4. The crystallites of ZSM-5 and mordenite were platelets with sizes around  $0.2 \mu\text{m}$  and  $0.4 \mu\text{m}$  respectively.

The composition of the methanol synthesis catalyst, its physicochemical properties and X-ray diffraction pattern are included in the supplementary information (Section 1). The degree of reduction of CuO after reaching the reaction temperature was  $>97\%$ . Only the XRD peaks of Cu and ZnO were observed after reduction.

#### 3.2 Catalytic performance

The conversion and selectivities for the methanol synthesis component alone are presented in Fig. 5. Methanol and carbon dioxide account for 96% and 3% of the products respectively at the conditions used. Methane and dimethyl ether were detected at trace levels with yields below 0.02%. A

slight decrease in the CO hydrogenation activity is observed during the first 6h on stream but the catalyst becomes stable thereafter. The conversions obtained at the different temperatures are low (< 4%) as a consequence of the high space velocities used and are far from thermodynamic equilibrium (38% at 250°C, 31% at 260°C and 24% at 270°C).

The CO conversions and selectivities to methanol, DME, hydrocarbons, and CO<sub>2</sub> obtained with physical mixtures of the Cu/ZnO/alumina catalyst with a zeolite are shown in Figs. 6 and 7. Higher CO<sub>2</sub> and H<sub>2</sub> concentrations are maintained through the water-gas shift (reaction 3) which removes the water formed in the dehydration reactions (reaction 5). The combination of the Cu/ZnO catalyst with a zeolite increases the total methanol synthesis rate due to more favourable kinetics for CO<sub>2</sub> hydrogenation [26], Fig. 6 and Fig. 7. Since the conversions are far from equilibrium, no thermodynamic synergy (i.e. lifting of equilibrium constraint on methanol synthesis) is observed under these experimental conditions. Dimethyl ether, olefins and paraffins were the only dehydration products detected in the gas phase. Paraffins are produced mainly from the hydrogenation of olefins over the Cu/ZnO catalyst rather than from acid catalysed hydride transfer. This was concluded from methanol synthesis experiments co-feeding ethylene where a complete conversion to ethane was observed (see supplementary information, Fig. F). The ratio paraffin to olefin was found to decrease as the molecular weight of the hydrocarbons increases, consistent with the steric hindrance by alkyl groups attached to the doubly bonded carbon atoms. It is worth noting that the significant production of hydrocarbons observed in Fig. 6 and Fig. 7 contrasts with the low levels of hydrocarbons and the corresponding high selectivity towards DME reported recently for hybrids containing zeolites [15]. The difference is attributed to the very low water concentrations obtained in the present work (below 0.1 bar) due to the low conversion levels, in comparison to studies conducted close to equilibrium conversions ( $p_{\text{water}} \sim 1.5$  bar). The higher water pressure has the effect of lowering the acidity thereby limiting hydrocarbon and coke formation. In addition, the interactions that arise from the proximity between the Cu/ZnO and the acidic functions are lower for physical mixtures [15] and therefore greater retention of acidity is expected.

All the catalyst mixtures tested undergo a kinetic induction period for hydrocarbon production in the beginning of the experimental runs. Such a phenomenon has been widely reported in methanol-to-hydrocarbon conversions and is ascribed to the gradual formation of organic species trapped in the zeolite (carbon-pool) that are the catalytic centres for methylation and olefin elimination reactions [27, 28].

### 3.3 Product distribution

The conversion and selectivity for the physical mixtures containing ZSM-5 and mordenite are presented in Fig. 6. It can be observed that the catalytic performance is strongly dependent on the time-on-stream and the reaction temperature. For ZSM-5, Fig 6(a), the initial selectivity towards DME is 88% of the organic products which decreases to 73% during the first 8h on stream at 250°C while the hydrocarbons increase from 4% to 17%. This coincides with the formation of entrained hydrocarbon species within the zeolite voids that build up from reactions involving DME and methanol. One hour after increasing the reaction temperature to 260°C, a steady selectivity was obtained in which DME and hydrocarbons represented 54% and 38% respectively. With a further increment in the temperature to 270°C, hydrocarbons became the main organic product (56%) to the detriment of DME (35%). For mordenite, Fig. 6(b), hydrocarbons are the main dehydration product after just 30 min of reaction at 250°C and their selectivity increases during the first 4h on stream. This fast induction period is attributed to the high acid strength (Fig. 2) and acid site density (Table 2) of MOR, and to the absence of spatial constraints inside the channels which facilitates the initial formation of organic species. Higher acid densities increase the probability for condensation reactions to occur, hence increasing the coking rate. Likewise, stronger acidity facilitates the formation of coke precursors and causes a more pronounced retention of coke molecules, leading to faster induction periods. As the deposited molecules become bulkier the acid sites are less accessible and the

diffusion of products from the pores is also more difficult. Consequently, dimethyl ether becomes the main organic product (55%) followed by hydrocarbons (34%). The water-gas shift rate decreases as less water is produced from dehydration reactions causing the CO conversion to plummet. Increasing the reaction temperatures to 260°C and 270°C does not appear to affect significantly the selectivities, Fig. 6(b). The relatively high hydrocarbon yields observed in Fig. 6 are in agreement with previous reports using physical mixtures containing ZSM-5 [16,17] and MOR [17].

The catalytic behaviours for the physical mixtures that contain the 10 atom-ring unidirectional (theta-1 and ZSM-23) and pseudo-unidirectional (FER) zeolites are shown in Fig. 7. Theta-1 and ferrierite exhibited similar conversion levels and the highest selectivity towards dimethyl ether. Conversions increased with temperature as expected and the selectivities remained almost constant. In both cases, DME accounts for ~85% of the organics produced while the contribution to the organics of methanol is 10% for FER and 13% for theta-1. Ferrierite produces slightly more hydrocarbons (5%) than theta-1 (2%) under these conditions, but this difference is relatively small considering that FER has around 20% more Brønsted sites than theta-1 and that the acid strength of ferrierite is higher, Table 2. With the higher density of acid sites in the ferrierite channels, the reaction products are more likely to undergo further chemical transformations along the diffusion paths. Considering that FER has a larger crystallite size compared to theta-1, it is apparent that the topology of ferrierite limits the formation of hydrocarbons, possibly by providing a preferential path for the diffusion of small reactants and products (i.e. methanol and dimethyl ether). In the case of ZSM-23 the initial DME selectivity was also high, around 81% of the organic products but, in contrast to FER and theta-1, selectivity to DME and CO conversion decreased continuously during the run while the selectivity to methanol increased.

The deactivation of ZSM-23 was more gradual than observed for mordenite. Although the methanol productivities are similar for the catalyst mixtures containing MOR and ZSM-23 (see supporting information Table C), most of the methanol formed in the presence of mordenite is transformed into DME and hydrocarbons while less than 50% is converted into dehydration products by the partially deactivated ZSM-23. This can be attributed to the higher density and strength of the acid sites of mordenite compared to ZSM-23, and the relative crystallites sizes. The low external surface area and large crystallites of ZSM-23 (Figure 4) creates long diffusion paths making the acid sites more difficult to access in the coked zeolite. The impact of carbon deposition on the loss of activity is discussed further in section 3.4 below.

The hydrocarbon product selectivities for the various tested mixtures at different temperatures are given in Table 3. Although in principle methane can be formed over the acid catalyst from surface methoxyl species [29], the yields obtained with the present catalyst mixtures are similar to those observed during the methanol synthesis alone over the Cu/ZnO/alumina suggesting that CH<sub>4</sub> is mainly formed over the metallic component from CO hydrogenation. For mordenite, ferrierite and theta-1, ethane is the most abundant hydrocarbon product, ZSM-5 produces similar amounts of ethane and propane, and ZSM-23 produces mainly C<sub>4+</sub> hydrocarbons. The selectivity towards bulkier hydrocarbons increases with temperature for all the zeolites but only aliphatic products were detected even at 270°C.

The organics retained on the spent zeolites were extracted with CH<sub>2</sub>Cl<sub>2</sub> after zeolite digestion. Analysis showed that the retained material consists mainly of alkylbenzenes, Fig. 8, which is in agreement with previous studies showing that methylbenzenes are active centres in MTH processes [30, 31]. In addition, studies using <sup>13</sup>C-methanol over ZSM-5 [28, 32] have suggested that while lower hydrocarbons (ethylene and propene) are mainly formed by reactions involving a methyl substituted aromatic ring, C<sub>4+</sub> olefins are formed by a competing route involving methylation and cracking of surface alkene chains. The mechanism controlling hydrocarbon formation is related to the topology of the zeolites [9, 11, 32, 33]. Remarkably, however, under the conditions used in the present study, similar high selectivities towards C<sub>2</sub> and C<sub>4+</sub> were obtained for ZSM-5, theta-1 and ZSM-23 suggesting that both mechanisms may be operating although the hydrocarbon yields are significantly lower for

theta-1 and ZSM-23. Moreover, the selectivity towards ethylene and propylene on FER and theta-1 decreases with time on stream while the  $C_{4+}$  selectivity increases. The loss of activity of the sites responsible for the formation of  $C_2$ - $C_3$  and  $C_{4+}$  products is different, indicating that they are likely to be formed by different mechanisms. For the unidirectional zeolites, it may be speculated that the steric effects limiting alkylbenzene formation inside the medium pores may be counteracted by the higher stability of the carbocations formed by the aromatic ring. Therefore, low amounts of polysubstituted benzenes may form on the exterior surface of theta-1 and ZSM-23. Regarding the  $C_2$  to  $C_3$  ratio, it has been reported that benzenes with up to four methyl groups eliminate predominantly ethylene while those with more substituents produce propene and butene [32]. For MOR, FER and theta-1, the higher abundance in the extracts of benzenes with up to four alkyls, Fig. 8, is consistent with the observed high selectivity towards ethane in the gaseous products. For ZSM-23 and ZSM-5 the relative amounts of low and highly substituted rings were similar, and consequently the selectivities to ethane and propane are observed to be closer. However, it is important to note that it is not possible to conclude based solely on the observation of the presence of alkylbenzenes as in Fig. 8 that these are active centres in the zeolites tested. For instance, Bjørgen et al. found that while hexamethylbenzene is catalytically active for MTH conversion over mordenite [34], it is unreactive over ZSM-5 [28].

### 3.4 Catalyst stability

The X-ray diffraction patterns for the zeolites recovered after reaction are shown in Fig. 9. Mordenite is not presented because it was not possible to separate the heavily coked particles from the mixture by visual inspection. The position of the diffraction peaks is consistent with those in Fig. 1 indicating that the crystal structures are maintained during reaction. Nevertheless, a decrease in the intensity of the reflections at low  $2\theta$  is noticeable for all the spent samples. Since low diffraction angles correspond to planes with low Miller indices that pass through the centre of channels [35], the decrease in the intensity is probably caused by carbonaceous material on the pore walls of the zeolites. The loss of aluminium from the framework of the zeolite is unlikely under the conditions of the experiments due to the low concentration of water in the reactor as noted above.

The coke content of the different catalysts was determined by TPO. For the methanol synthesis components  $CO_2$  evolved in two regions: one between 200 and 300°C, and a high temperature peak with a maximum around 710°C that corresponds to graphitic carbon used to shape the commercial pellets of the commercial Cu/ZnO/alumina catalyst (see supplementary information, Table A and Fig. B and C). The amount of  $CO_2$  at low temperature was around  $0.3 \mu\text{mol}\cdot\text{mg}^{-1}$  for the Cu catalysts which is low in comparison to other reported values [36, 37]. This is assumed to be a consequence of the relatively high space velocities and the excess of  $H_2$  used in the present experiments.

The TPO profiles of the spent zeolites are presented in Fig. 10. The total coke contents and the coke selectivities in the conversion of methanol are given in Table 4. In the case of mordenite, it was impossible to separate the components from the spent mixture so the analysis was carried over a sample containing both catalysts. For spent MOR,  $CO_2$  was detected over a wide range of temperatures, but the main contribution had a maximum at 625°C. Considering the low combustion temperatures of the compounds deposited over the spent Cu catalysts (see above), the 625°C peak was assigned to bulky polyaromatics located in the wide pores of mordenite. This heavy coke is not soluble in  $CH_2Cl_2$ , hence it was not detected in the GC-MS analysis of the extracts, Fig. 8. Additionally, diffusion restrictions may arise from the pseudo-unidimensional channel structure of MOR contributing to such a high decoking temperature [38]. In any case, the significant amount of carbonaceous species deposited over mordenite, Table 4, reduces the number of catalytic sites available and restricts the mass transport of reactants and products causing the steep decrease in the observed CO conversion, Fig. 6(b). In the case of spent ZSM-5,  $4.4 \text{ mmol}\cdot\text{g}^{-1}$  of  $CO_2$  were evolved in a broad range of temperatures (200 – 675°C) corresponding to polycyclic hydrocarbons with varying

hydrogen content. The relatively high stability of ZSM-5 observed in CO hydrogenation, Fig. 6(a), stems from a restricted transition-state for the formation of bulky carbon molecules within its pores. A hydrogen deficient coke layer is formed mainly on the external surface of the ZSM-5 crystallites leaving the acid sites in the channels accessible for catalysis [28, 38, 39].

The oxidation of the carbonaceous compounds on the spent FER occurs in two distinctive stages: 365°C (alkylbenzenes) and 495°C (light polyaromatics). The total amount of CO<sub>2</sub> produced is a comparatively low value and evidently very bulky carbon species are not formed. This contributes to the good stability observed in Fig. 7(a) which is in agreement with previous reports [12-15]. Coke oxidation for theta-1 and ZSM-23 occurs mainly in the high temperature range with a maximum at 730°C corresponding to graphitic coke. Since the catalytic tests were conducted at low temperatures where graphitisation of carbonaceous deposits is not expected, graphite is assumed to be formed during TPO from a combination of restricted diffusion and enhanced dehydrogenation of coke as the temperature is increased. This interpretation is supported by the presence of significant quantity of alkyl benzenes in the compounds extracted from both spent zeolites, Fig. 8, and by the production of water during TPO without any parallel evolution of CO<sub>2</sub> in the temperature range corresponding to polyaromatics, Fig. 10. It has been reported that below ca. 475°C the oxidation of the carbon component of coke is chemically controlled while the hydrogen component is readily combusted [40]. Therefore, due to the diffusional constraints in theta-1 and ZSM-23, the oxygen molecules that reach the carbonaceous deposits will react mainly with hydrogen creating unsaturations that will eventually lead to graphitic coke, which is more difficult to burn. A similar shift of the CO<sub>2</sub> maxima towards higher temperatures was obtained for mordenite and reveals the existence of significant diffusion limitations in the coked catalyst.

To clarify the nature of the carbonaceous deposits on theta-1 and ZSM-23, EPR analysis of the spent zeolite samples was performed. The samples showed a symmetric sharp signal centred at about 335 mT with no hyperfine splitting, which was much stronger in the spectrum from spent ZSM-23 (see supplementary information, Fig. G and H). This signal has been assigned previously to highly unsaturated polyaromatic radicals associated with high temperature coke [41], or related hydrocarbon peroxy radicals as the present samples were exposed extensively to air prior to EPR. Since graphite compounds exhibit quite different signals [41, 42], EPR provides confirmatory evidence that graphitic coke was not formed during the catalytic tests.

The high selectivity of ZSM-23 towards coke compared to that obtained for theta-1 and FER (Table 4) is striking considering their similarity in dimensionality, channel widths and relative acidity. However, some significant differences in the zeolite samples are apparent in the nitrogen adsorption isotherms (Fig. 3) and the SEM images (Fig. 4). The crystallites of theta-1 and ZSM-23 have the same small rod-like morphology, but the crystallites of ZSM-23 are significantly larger. With increasing crystallite size, the diffusion paths of molecules inside the pores are lengthened. This leads to the formation and accumulation of less-volatile carbon species on ZSM-23, which is confirmed by the delay in the H<sub>2</sub>O signal observed in the TPO profile of ZSM-23 compared to theta-1 (Fig. 10). The bulky organics that accumulate gradually inside the channels decrease the accessibility of methanol to the dehydration sites causing loss of activity and a corresponding rise in selectivity to methanol, Fig. 7(c).

Ferrierite, on the other hand, presents a completely different morphology although the average crystallite size is similar to that of ZSM-23, Fig. 4(a). Based on the Lennard-Jones dimensions of the organics detected in the gas phase [43], the narrow channels running across the medium pores of ferrierite offer enough space for diffusion of methanol, DME, methane and ethane (ethylene) exclusively. Consequently, the formation of coke and hydrocarbons is prevented since methanol and DME are unlikely to find alkylbenzene centres along these narrow channels. The existence of a preferential channel for small molecules that is not severely blocked by coke is consistent with the lower diffusional constraints observed during the temperature programmed

oxidation of carbonaceous deposits on the spent ferrierite. As mentioned above the burning rate of hydrogen is taken to be controlled by oxygen diffusion while carbon combustion is chemically controlled. Therefore, the existence of an additional diffusion path in the ferrierite provides enough oxygen to oxidise the carbon at lower temperatures, preventing graphitisation, Fig. 10.

Although there is a broad correlation between the decrease in the dehydration activity and the amount of carbon deposited on the zeolites, from the results presented above it is clear that the deactivation trends cannot be explained exclusively by this parameter. In particular, ZSM-23 shows a significant deactivation in spite of the relatively low amount of coke detected Table 4. The deactivation of the zeolites during the syngas-to-DME reactions over physical mixtures is a shape-related phenomenon determined by the pore structure and the crystallite size of the zeolites used. This observation is in agreement with methanol dehydration studies reported recently by García-Trenco et al. at temperatures relevant for STD but at significantly lower pressures [15]. However, the authors did not observe any correlation between the dehydration activity and the topology of the zeolites. The present results, on the other hand, indicate that the nature of the entrained organics depends on the pore structure of the zeolite and dictates the by-product distribution during the single-stage synthesis of DME. Over the physical mixtures studied here no correlation was found between larger external surface areas and the loss of dehydration activity, such as that reported by García-Trenco et al. for hybrid catalysts [15,44]. The detrimental interaction between the metallic and the acidic components has been shown to be a major cause of deactivation of STD hybrid catalysts [15]. However, the limited contact area between the Cu/ZnO catalyst and the zeolites in the physical mixture decreases the impact of this mode of deactivation as pointed out earlier by García-Trenco et al. [44]. Therefore, for physical mixtures of Cu/ZnO/Al<sub>2</sub>O<sub>3</sub> and zeolites under CO rich syngas, deactivation of the dehydration function is dominated by carbon formation. Deactivation by proximity has been shown to be relevant, however, in physical mixtures containing  $\gamma$ -alumina as the dehydration function [45].

#### 4. Conclusions

During the single-stage synthesis of dimethyl ether from CO rich syngas, the formation of hydrocarbons over physical mixtures of Cu/ZnO/Al<sub>2</sub>O<sub>3</sub> and H-zeolites is related to the deposition of carbonaceous compounds on the surface of the zeolites. The entrained alkylbenzenes and the stability and selectivity were found to depend on the topology of the zeolite used. Dimethyl ether was the main dehydration product obtained over ferrierite and the unidirectional zeolites. FER and theta-1 were found to be the most selective and stable catalysts over the whole range of temperature tested. The lower stability of ZSM-23 appears to be related to its larger crystallite size which imposes diffusion constraints for products and reactants, favouring the formation and the accumulation of less volatile species. Mordenite and ZSM-5 can accommodate bulky species within the pores and the channel intersections resulting in a significant deactivation and in a relatively high production of hydrocarbons to the detriment of the DME selectivity.

#### Acknowledgement

R. Montesano thanks CONACYT and SEP for a scholarship award. A. Narvaez thanks Universidad Católica de la Santísima Concepción for the support received. The authors are grateful to Dr. Sami Barri from Imperial College London for his help in the preparation of theta-1 and ZSM-23 and to Dr. Enrico Salvadori and Prof. Chris Kay from the Department of Chemistry, University College London for conducting the EPR measurements. We thank EPSRC for an equipment grant.

#### References

- [1] F. Sousa-Aguiar, L. G. Appel, in: J. J. Spivey, K. M. Dooley (Eds.), *Specialist Periodical Reports: Catalysis* Vol. 23, RSC, 2011, p. 284-315
- [2] M. M. Mench, H. M. Chance, C. Y. Wang, *J. Electrochem. Soc.* 151 (2004) A144-A150

- [3] A. C. Sofianos, M. S. Scurrall, *Ind. Eng. Chem. Res.* 30 (1991) 2372-2378
- [4] M. Xu, J. H. Lunsford, D. W. Goodman, A. Bhattacharyya, *Appl. Catal., A* 149 (1997) 289-301
- [5] D. Mao, W. Yang, J. Xia, B. Zhang, Q. Song, Q. Chen, *J. Catal.* 230 (2005) 140-149
- [6] C.D. Chang, W. H. Lang, A. J. Silvestri, US Patent 4,062,905 (1977)
- [7] C. D. Chang, in: C. Song, J. M. Garcés, Y. Sugi (Eds.) *Shape-Selective Catalysis*, ACS Symposium Series 738. ACS, 1999, 96-114
- [8] G. F. Froment, W. J. H. Dehertog, A. J. Marchi, in: J. J. Spiver (Ed.), *Specialist Periodical Reports: Catalysis Vol. 9*, RSC, 1992, 1-64
- [9] J. F. Haw, W. Song, D. M. Marcus, J. B. Nicholas, *Acc. Chem. Res.* 36 (2003) 317-326
- [10] S. Jiang, Y. K. Hwang, S. H. Jhung, J. -S. Chang, J. -S. Hwang, T. Cai, S.-E. Park, *Chem. Lett.* 33 (2004) 1048-1049
- [11] S. Teketel, W. Skistad, S. Benard, U. Olsbye, K. P. Lillerud, P. Beato, S. Svelle, *ACS Catal.* 2 (2012) 26-37
- [12] P. S. Sai Prasad, J. W. Bae, S. -H. Kang, Y. J. Lee, K.-W. Jun, *Fuel Process. Technol.* 89 (2008) 1281-1286
- [13] J. H. Flores, D. P. B. Peixoto, L. G. Appel, R. R. de Avillez, M.I. Pais da Silva, *Catal. Today* 172 (2011) 218-225
- [14] L. G. Appel, A. M. D. De Farias, A. M. L. Esteves, M. A. Fraga, F. S. R. Barbosa, L. E. P. Borges, J. L. F. Monteiro, J. H. Flores, M. I. Pais da Silva, E. F. Sousa-Aguiar, U.S. Patent 20090326281 (2009), to Petroleo Brasileiro.
- [15] A. García-Trenco, S. Valencia, A. Martínez, *Appl. Catal., A* 468 (2013) 102-111
- [16] D. Mao, J. Xia, B. Zhang, G. Lu, *51 Energy Convers. Manage.* (2010) 1134-1139
- [17] M. Stiefel, R. Ahmad, U. Arnold, M. Döring, *Fuel Process. Technol.* 92 (2011) 1466-1474
- [18] S. A. I. Barri, P. Howard, C. D. Telford *Eur. Patent 0057049* (1982), to British Petroleum
- [19] S. A. I. Barri *GB Patent 2190910* (1987), to British Petroleum
- [20] P. Magnoux, P. Roger, C. Canaff, V. Fouche, N. S. Gnep, M. Guisnet, *Stud. Surf. Sci. Catal.* 34 (1987) 317-330
- [21] S. A. I. Barri, G. W. Smith, D. White, D. Young, *Nature* 312 (1984) 533-534
- [22] D. Zhang, S. A. I. Barri, D. Chadwick, *Appl. Catal., A* 403 (2011) 1-11
- [23] N. Katada, H. Igi, J. Kim, M. Niwa, *J. Phys. Chem. B* 101 (1997) 5969-5977
- [24] F. Rouquerol, J. Rouquerol, K. Sing, *Adsorption by Powders and Porous Solids*, Academic Press, London, 1999
- [25] G. Leofanti, M. Padovan, G. Tozzola, B. Venturelli, *Catal. Today* 41 (1998) 207-219
- [26] K. M. Vaden Bussche, G. F. Froment, *J. Catal.* 161 (1996) 1-10

- [27] I. M. Dahl, S. Kolboe, *J. Catal.* 149 (1994) 458-464
- [28] M. Bjørgen, S. Svelle, F. Joensen, J. Nerlov, S. Kolboe, F. Bonino, L. Palumbo, S. Bordiga, U. Olsbye, *J. Catal.* 249 (2007) 195-207
- [29] G. J. Hutchings, R. Hunter, *Catal. Today* 6 (1990) 279-306
- [30] Ø. Mikkelsen, P. O. Rønning, S. Kolboe, *Microporous Mesoporous Mater.* 40 (2000) 95-113
- [31] W. Song, H. Fu, J. F. Haw, *J. Am. Chem. Soc.* 123 (2001) 4749-4754
- [32] S. Svelle, U. Olsbye, F. Joensen, M. Bjørgen, *J. Phys. Chem. C* 111 (2007) 17981-17984
- [33] U. Olsbye, S. Svelle, M. Bjørgen, P. Beato, T. V. W. Janssens, F. Joensen, S. Bordiga, K. P. Lillerud, *Angew. Chem. Int. Ed.* 51 (2012) 5810-5831
- [34] M. Bjørgen, S. Akyalcin, U. Olsbye, S. Benard, S. Kolboe, S. Svelle, *J. Catal.* 275 (2010) 170-180
- [35] M. M. J. Treacy, J. B. Higgins, *Collection of Simulated XRD Powder Patterns for Zeolites*, 4<sup>th</sup> ed., Elsevier, Amsterdam, 2001
- [36] A. T. Aguayo, J. Ereña, I. Sierra, M. Olazar, J. Bilbao, *Catal. Today* 106 (2005) 265-270
- [37] F. S. T. Barbosa, V. S. O. Ruiz, J. L. F. Monteiro, R. R. de Avillez, L. E. P. Burges, L. G. Appel, *Catal. Lett.* 126 (2008) 173-178
- [38] P. Dejaive, A. Auroux, P. C. Gravelle, J. C. Védrine, *J. Catal.* 70 (1981) 123-136
- [39] D. Mores, E. Stavitski, M. H. F. Kox, J. Kornatowski, U. Olsbye, B. M. Weckhuysen, *Chem. Eur. J.* 14 (2008) 11320-11327
- [40] J. B. Butt, E. E. Petersen, *Activation, Deactivation, and Poisoning of Catalysts*, Academic Press, London, 1988
- [41] H. G. Karge, J. -P. Lange, A. Gutsze, M. Łaniecki, *J. Catal.* 114 (1988) 144-152
- [42] L. S. Singer, G. Wagoner, *Electron Spin Resonance in High-Temperature Carbons and Graphites*, Proc. Fifth Conference on Carbon, University Park, PA, 19-23 June 1961, Pergamon, New York, 1962, 37-64
- [43] C. E. Gounaris, C. A. Floudas, J. Wei, *Chem. Eng. Science*, 61 (2006) 7933-7948
- [44] A. García-Trenco, A. Vidal-Moya, A. Martínez, *Catal Today* 179 (2012) 43-51
- [45] R. Montesano, D. Chadwick, *Catal. Commun.* 29 (2012) 137-140

**Table 1.** Textural properties of the zeolites

Catalyst	Type	$S_{\text{BET}}$ ( $\text{m}^2\cdot\text{g}^{-1}$ )	$S_{\text{ext}}$ ( $\text{m}^2\cdot\text{g}^{-1}$ )	Pore volume ( $\text{cm}^3\cdot\text{g}^{-1}$ )
ZSM-5 (CBV 5524G)	MFI	404	41	0.173
Mordenite (CBV 21A)	MOR	432	51	0.158
Ferrierite (CP 914)	FER	308	42	0.124
Theta-1	TON	208	38	0.079
ZSM-23	MTT	204	15	0.071

**Table 2.**  $\text{SiO}_2/\text{Al}_2\text{O}_3$  ratios and  $\text{NH}_3$  desorption properties of the zeolites

Catalyst	$\text{SiO}_2/\text{Al}_2\text{O}_3$ (mol/mol)	Framework site concentration ( $\text{mmol}\cdot\text{g}^{-1}$ ) <sup>a</sup>	LT ammonia desorption ( $\text{mmol}\cdot\text{g}^{-1}$ )	HT ammonia desorption ( $\text{mmol}\cdot\text{g}^{-1}$ )
ZSM-5 (CBV 5524G)	50	0.64	0.32	0.52
Mordenite (CBV 21A)	20	1.54	0.44	1.02
Ferrierite (CP 914)	55	0.59	0.41	0.60
Theta-1	63	0.52	0.30	0.50
ZSM-23	68	0.48	0.32	0.47

a. Calculated based on  $\text{SiO}_2/\text{Al}_2\text{O}_3$  ratios

**Table 3.** Hydrocarbon distributions for ZSM-5, MOR, FER, theta-1 and ZSM-23 at different temperatures.<sup>a</sup>

HC fraction (mol %)	ZSM-5	MOR	FER	Theta-1	ZSM-23
Reaction temperature 250°C					
C <sub>1</sub>	2.7	9.0	5.3	6.0	24.7
C <sub>2</sub>	29.9	70.1	85.0	71.9	10.3
C <sub>3</sub>	34.1	4.3	2.2	4.1	11.4
C <sub>4</sub>	14.6	12.7	2.6	3.3	14.6
C <sub>5</sub>	10.5	3.9	4.8	14.7	39.0
C <sub>6+</sub>	8.2	0.0	0.0	0.0	0.0
Reaction temperature 260°C					
C <sub>1</sub>	1.9	8.2	12.2	11.7	22.8
C <sub>2</sub>	24.0	72.5	72.0	45.1	10.0
C <sub>3</sub>	35.3	4.1	3.1	8.9	15.8
C <sub>4</sub>	13.4	11.3	4.3	10.4	18.6
C <sub>5</sub>	8.6	3.9	8.3	18.6	27.5
C <sub>6+</sub>	16.8	0.0	0.0	5.3	5.2
Reaction temperature 270°C					
C <sub>1</sub>	1.5	7.6	15.4	16.4	22.1
C <sub>2</sub>	25.1	74.8	61.9	41.0	10.8
C <sub>3</sub>	34.9	4.8	4.6	10.7	15.4
C <sub>4</sub>	13.6	8.8	6.0	10.7	18.6
C <sub>5</sub>	9.1	4.1	8.5	15.6	23.6
C <sub>6+</sub>	15.7	0.0	3.5	5.6	9.5

a. Values at 250°C, 260°C and 270°C correspond to TOS 8, 22 & 30h

---

respectively

**Table 4.** Coke content in the spent zeolites and coke selectivity

Catalyst	Coke content (mmol·g <sup>-1</sup> )	Coke selectivity <sup>a</sup> (mg <sub>C</sub> ·g <sub>MeOH</sub> <sup>-1</sup> )
ZSM-5	4.4	4.6
Mordenite <sup>b</sup>	11.8	19.2
Ferrierite	2.5	2.8
Theta-1	3.4	3.7
ZSM-23	3.3	10.9

a. Defined as the mass of carbon deposited per total mass of methanol converted (DME + hydrocarbons + coke)

b. Includes the carbon in Cu/ZnO/Al<sub>2</sub>O<sub>3</sub>

Figure captions

**Fig. 1.** XRD patterns of the fresh zeolites used in the catalyst mixtures

**Fig. 2.** NH<sub>3</sub>-TPD profiles of the fresh zeolites: mordenite, ferrierite, ZSM-23, theta-1 and ZSM-5

**Fig. 3.** Nitrogen adsorption and desorption isotherms at 77 K for FER, theta-1 and ZSM-23

**Fig. 4.** Scanning electron microscopy images of a) ferrierite, b) theta-1, c) ZSM-23

**Fig. 5.** CO conversion and selectivities for the Cu/ZnO catalyst alone. Methanol ▲, DME □, hydrocarbons + and CO<sub>2</sub> ●. Conditions: H<sub>2</sub>/CO = 2, P = 3 MPa, SV = 8400 h<sup>-1</sup>, temperatures in figure caption

**Fig. 6.** CO conversion and selectivities for the a) Cu/ZnO + ZSM-5, b) Cu/ZnO + MOR. Methanol ▲, DME □, hydrocarbons + and CO<sub>2</sub> ●. Conditions: H<sub>2</sub>/CO = 2, P = 3 MPa, SV = 8400 h<sup>-1</sup>, temperatures in figure captions

**Fig. 7.** CO conversion and selectivities for the a) Cu/ZnO + FER, b) Cu/ZnO + theta-1, c) Cu/ZnO + ZSM-23. Methanol ▲, DME □, hydrocarbons + and CO<sub>2</sub> ●. Conditions: H<sub>2</sub>/CO = 2, P = 3 MPa, SV = 8400 h<sup>-1</sup>, temperatures in figure captions

**Fig. 8.** GC-MS analyses of the retained material in the spent zeolites: mordenite, ferrierite, ZSM-23, theta-1 and ZSM-5

**Fig. 9.** XRD patterns of the zeolites recovered after reaction

**Fig. 10.** TPO profiles for the spent acid catalysts. Conditions:  $\beta = 10^{\circ}\text{C}\cdot\text{min}^{-1}$ , 10% O<sub>2</sub>/Ar = 45 mL·min<sup>-1</sup>. CO<sub>2</sub> = m/z 44 (solid line), H<sub>2</sub>O = m/z 18 (dashed line)

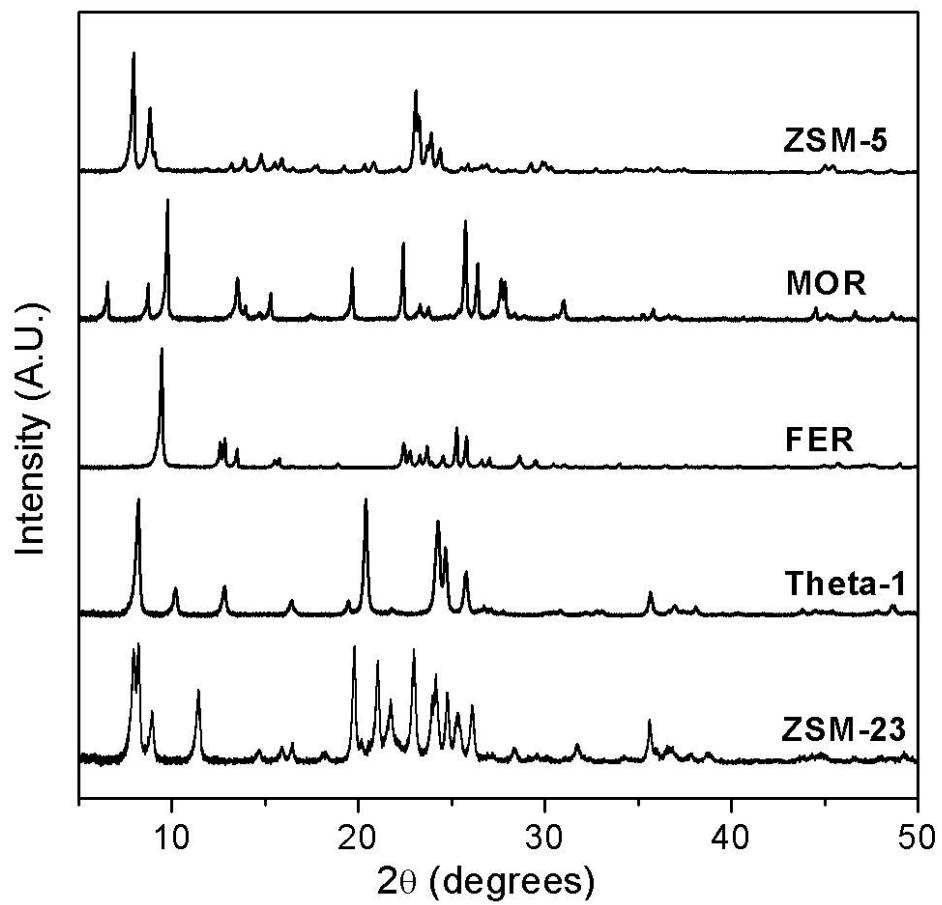


Figure 1

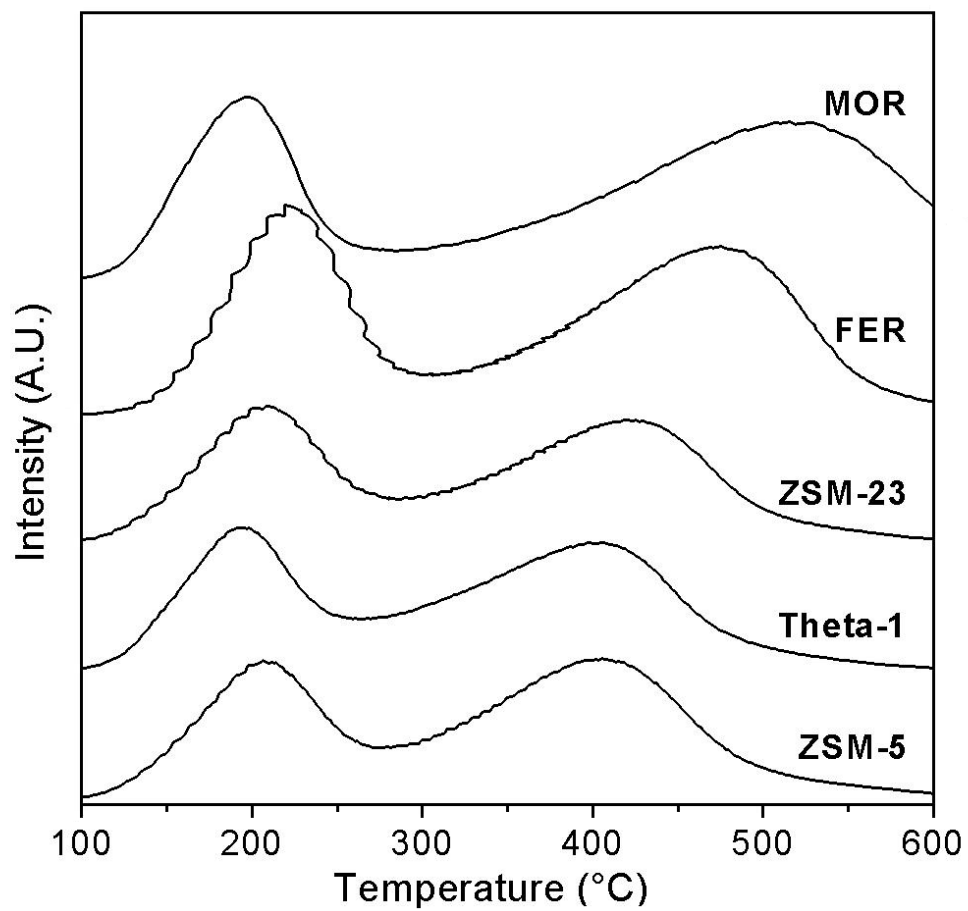


Figure 2

ACCEPTED

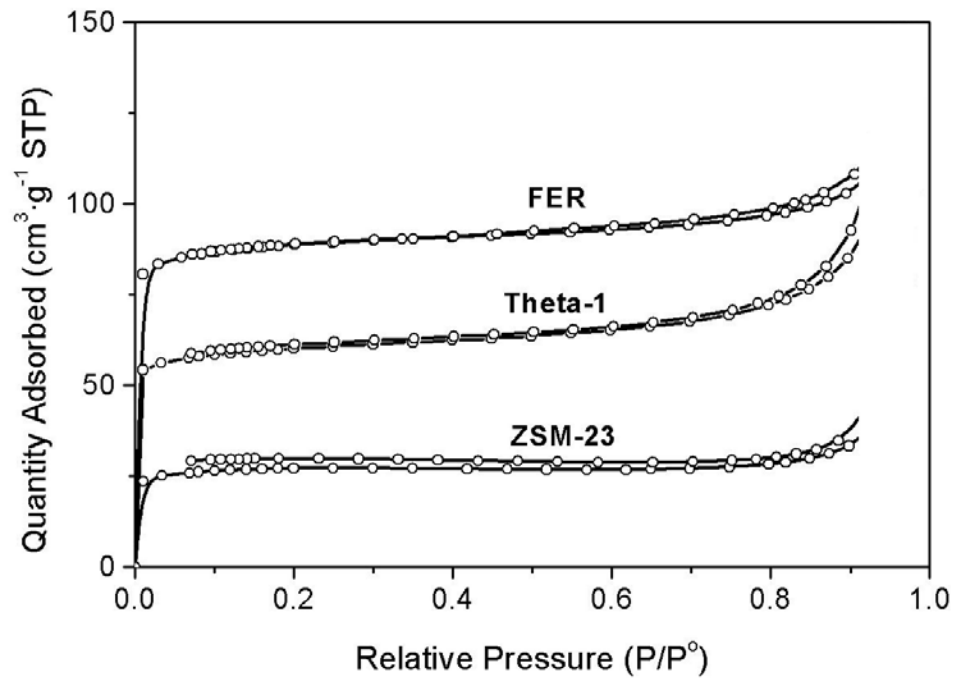


Figure 3

Accepted Manuscript

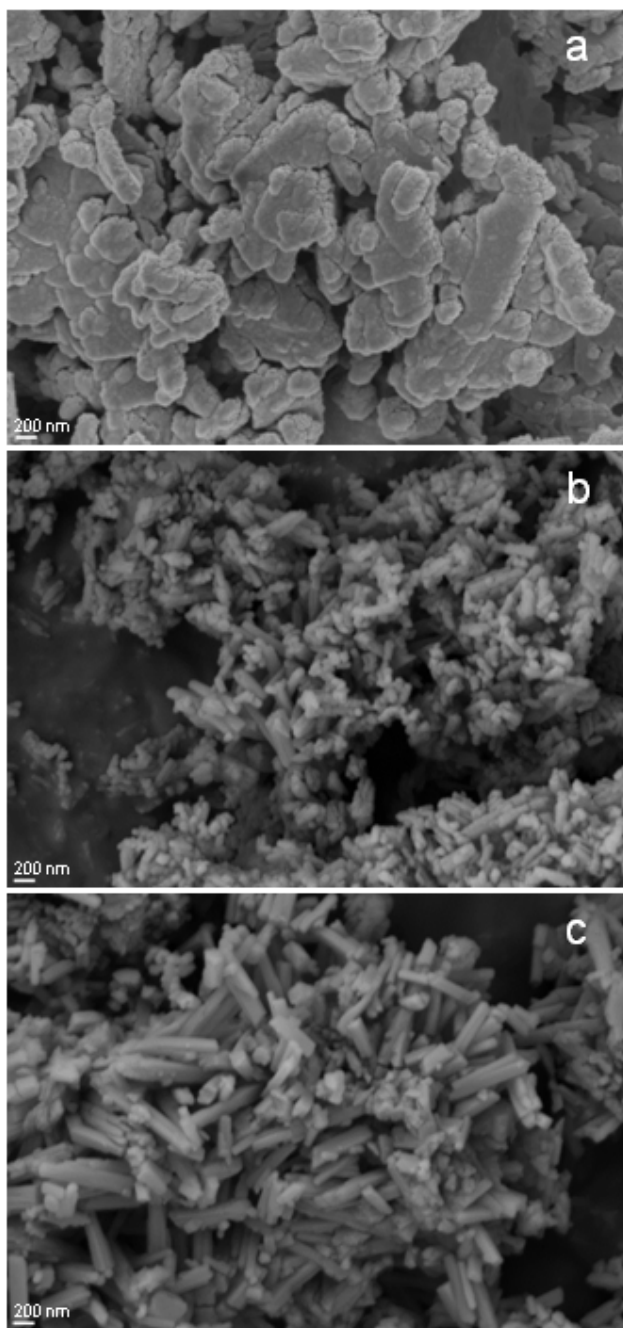


Figure 4

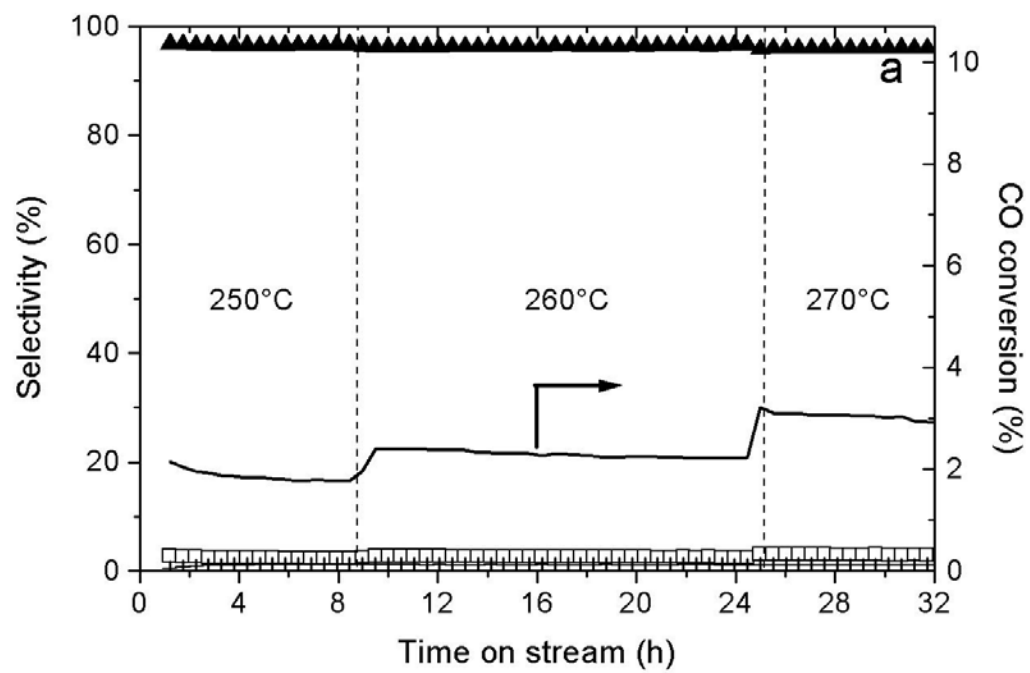


Figure 5

Accepted Manuscript

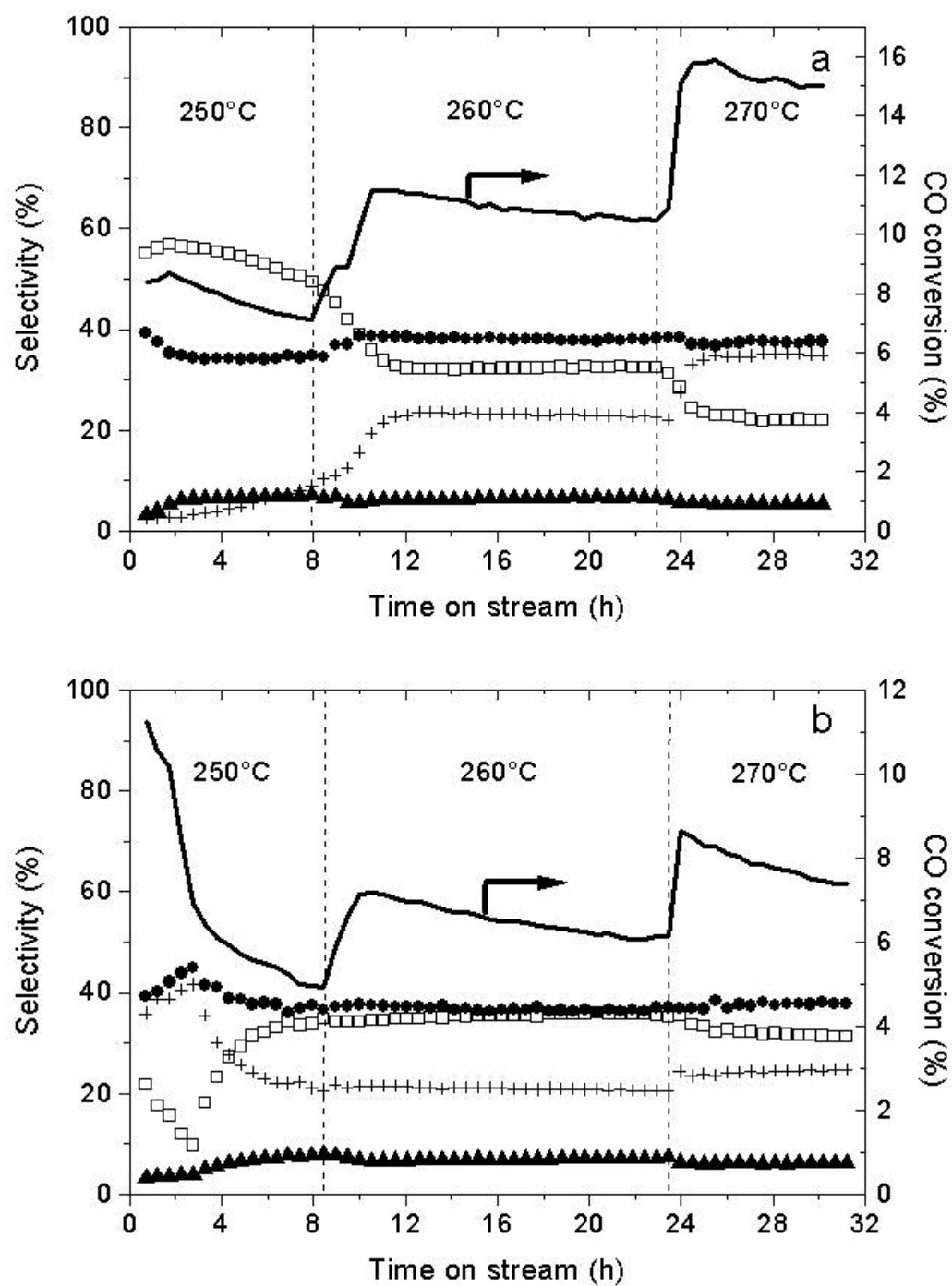


Figure 6

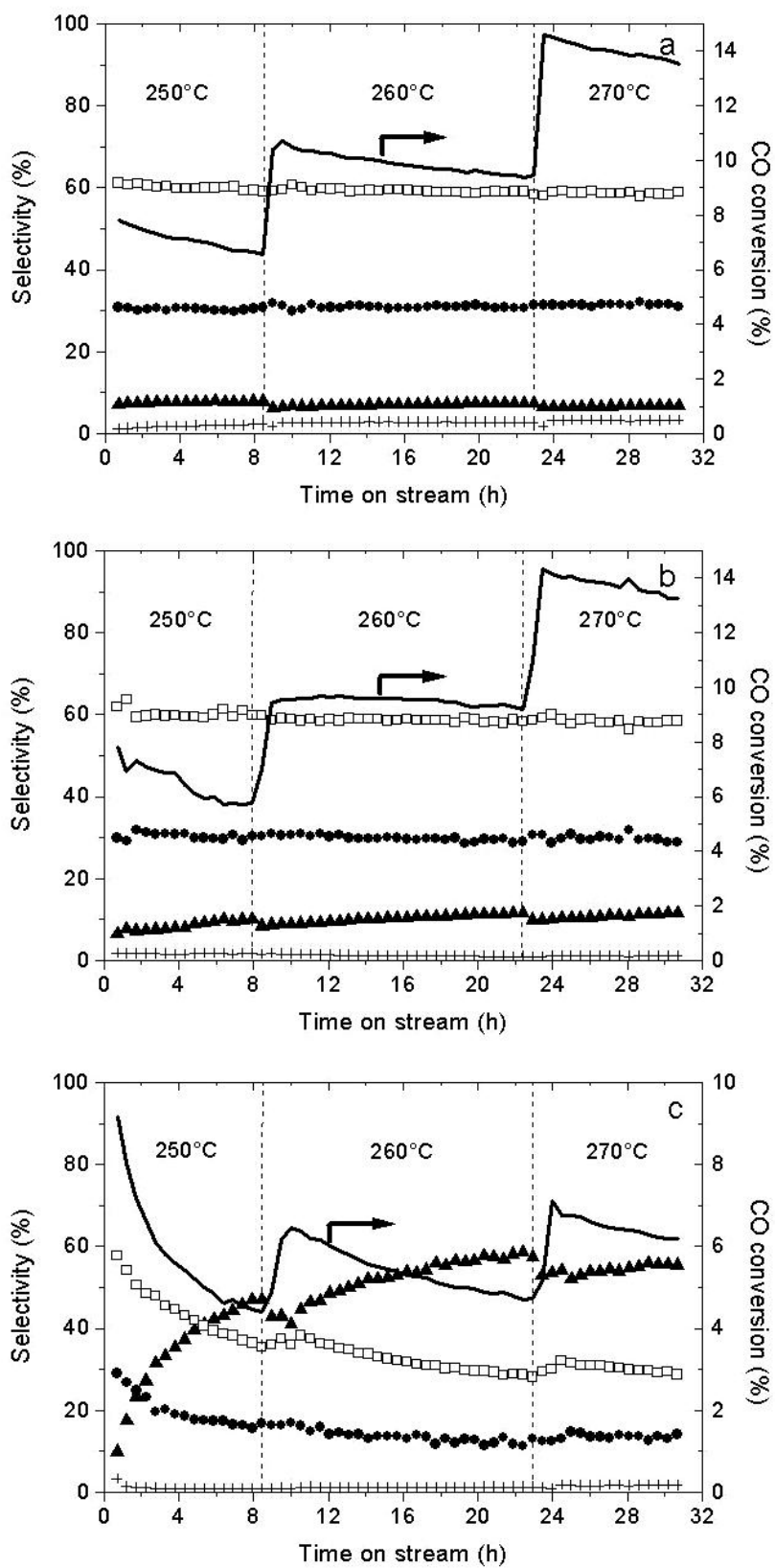


Figure 7

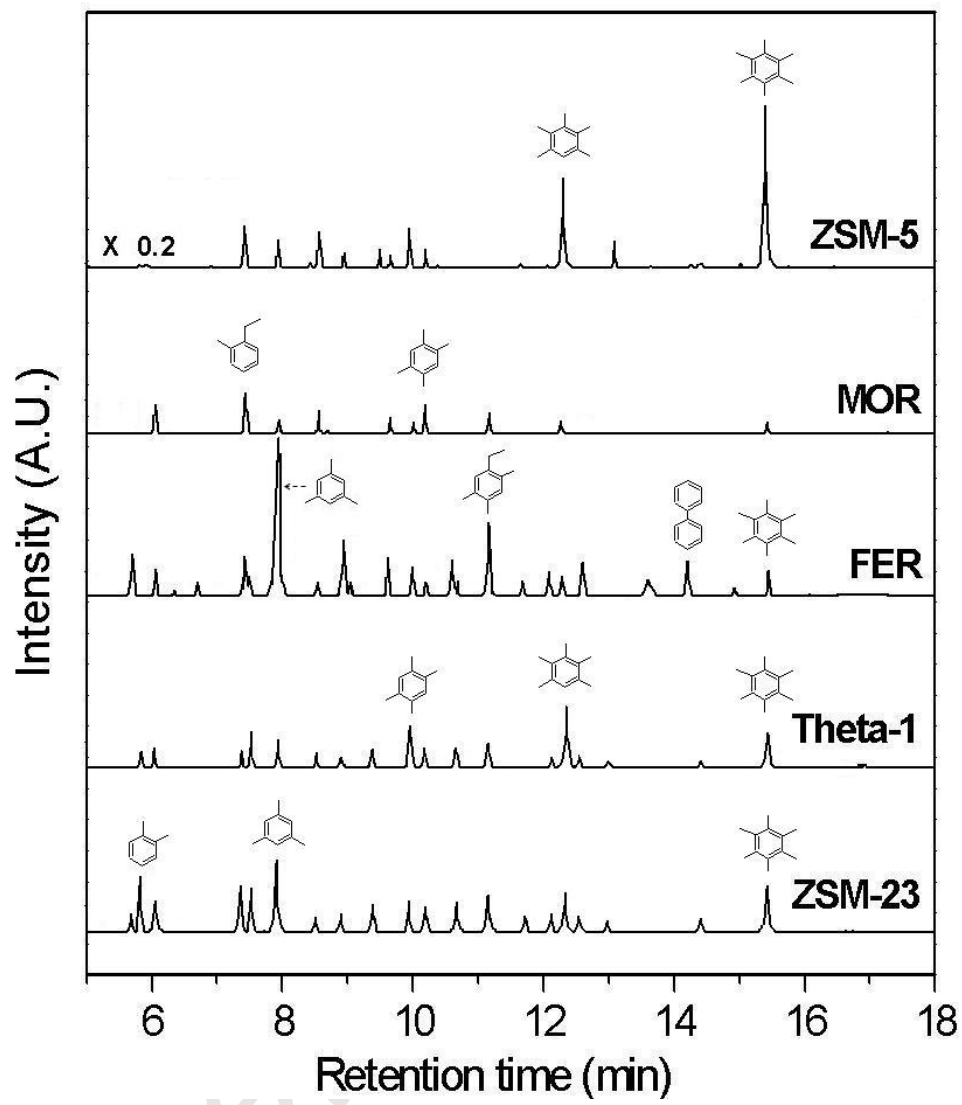


Figure 8

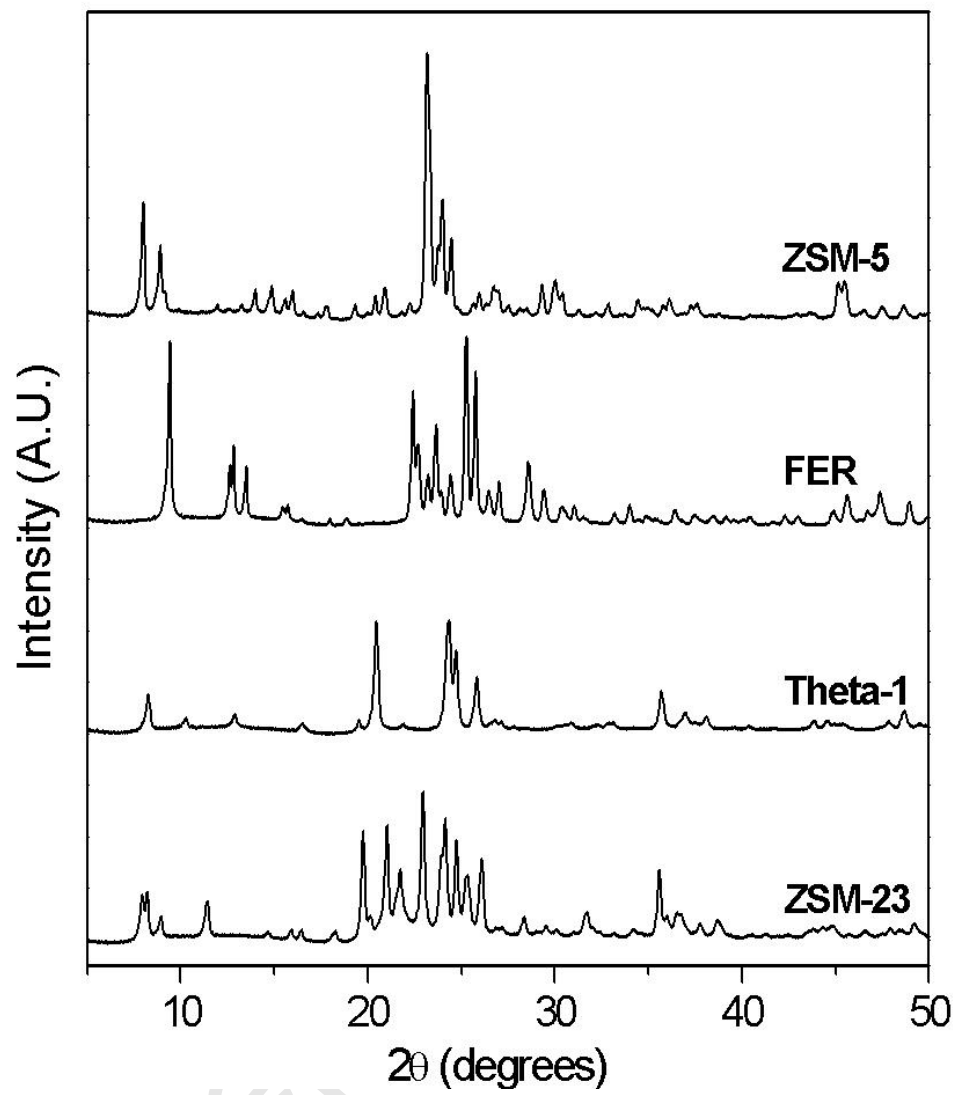


Figure 9

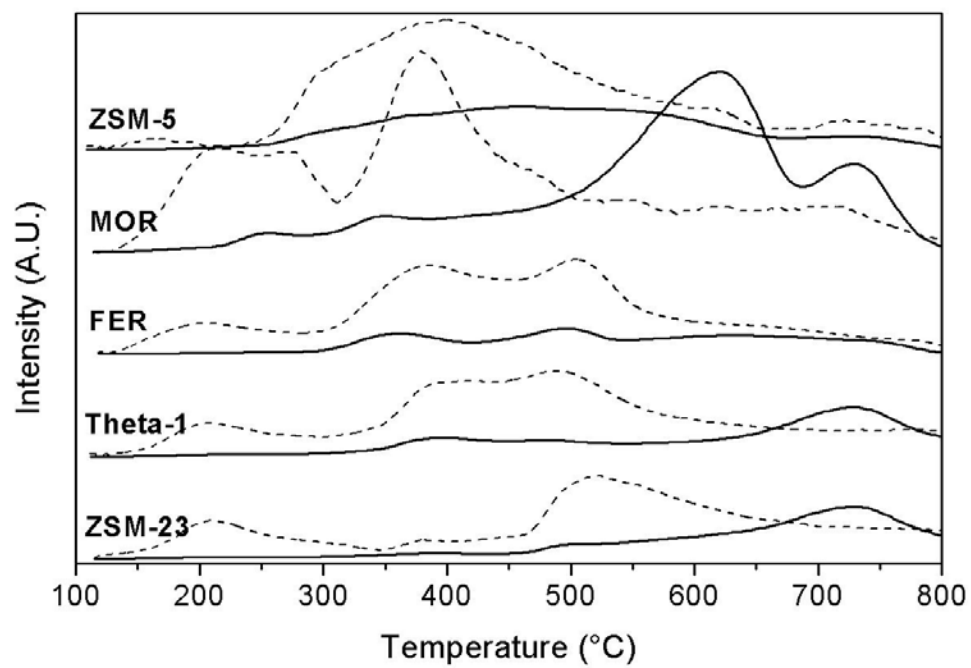


Figure 10

ACCEPTED MANUSCRIPT

